

Figure 1: Schematic CSC chamber, indicating the local coordinate system.

## 1 Introduction

The muon endcap was aligned using information from four different sources: photogrammetry, the Muon Endcap Alignment System, tracks from beam-halo muons, and tracks from collisions muons. Some of these sources of information are orthogonal, while others provide for cross-checks between the different systems. To combine information, alignment corrections were applied in a well-defined sequence, such that each step benefits from the previous. Potentially interdependent corrections were iterated to obtain a mutually consistent solution.

Below are the sources of alignment information and the order of their application. Global CMS coordinates are defined in [ref]; local coordinates are defined with respect to the CSC chambers, with  $x$  pointing approximately in the global  $r\phi$  direction,  $y$  in the radial direction away from the beamline, and  $z$  collinear with CMS global  $z$ . Rotation angles  $\phi_x$ ,  $\phi_y$ , and  $\phi_z$  are rotations around the corresponding local axes. (See Fig. 1 for a diagram of relevant coordinates.)

1. Photogrammetry [ref]: alignment derived from a set of photographs taken in 2007, establishing local coordinates  $x$ ,  $y$ ,  $z$ ,  $\phi_x$ , and  $\phi_z$  for chambers relative to the disks on which they are mounted. Two points were measured on each chamber, and these points are on the local  $y$  axis (hence the  $\phi_y$  degree of freedom is unavailable). The disks have subsequently been moved, with all chambers attached.
2. Muon Endcap Alignment System [ref]: a system of three lasers crossing the face of each disk, six lasers parallel with the beamline crossing all disks, and calipers measuring the  $z$  spacing between disks. This system is highly sensitive to the large displacements and bowing of disks in the CMS magnetic field, and therefore supplied corrections to the photogrammetry measurement from the zero-field state to the full-field state in local  $\phi_x$  and  $z$ .
3. Entrance angles of tracks from the tracker: systematic discrepancies between the entrance angles predicted by muons from the tracker and entrance angles measured by the muon chambers themselves were used to determine  $\phi_y$ .

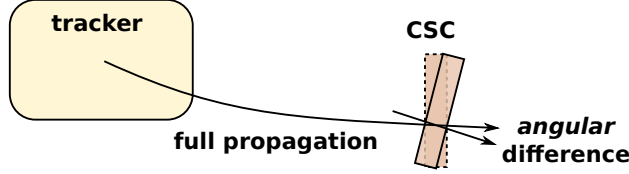


Figure 2: Schematic of CSC  $\phi_y$  alignment using tracks from the tracker.

4. Chamber alignment with beam-halo muons [ref]: relative local  $x$  and  $\phi_z$  of chambers derived from beam-halo tracks passing through pairs of adjacent chambers. Since the tracks are propagated short distances through low density material, propagation errors are minimal, but since the measurements have no external reference, the results are only valid for relative positions of chambers within each CSC ring.
5. Ring alignment with collisions muons: global  $x$ ,  $y$ , and  $\phi_z$  corrections for pre-aligned rings relative to the CMS tracker. Tracks were propagated through material and inhomogeneous magnetic fields, but the alignment was simplified by the assumption that each ring is internally well-aligned.

The geometry produced after step #5 was cross-checked using beam-halo muons propagated through the whole endcap (sensitive to a different set of systematic uncertainties), and steps #4 and #5 were iterated for mutual consistency.

## 2 Measurement of disk bending with the Muon Endcap Alignment System

### 3 Alignment of $\phi_y$ angles

Several attempts were made to align the  $\phi_y$  angles of chambers, but method with the most precision and fewest assumptions uses tracks propagated from the tracker. All track parameters are determined by the tracker, and the full CMS propagation model is used to estimate how a muon with a given trajectory will navigate through the material and magnetic field to the CSC chambers. In each chamber, the propagated  $dx/dz$  entrance angle of the track is compared with the entrance angle measured by the chamber, and systematic differences are interpreted as a misalignment of the chamber (Fig. 2). Entrance angles are less sensitive to potential propagation errors than positions, and the interpretation of discrepancies as chamber misalignments was verified in extreme cases by the fact that track-chamber differences (“residuals”) are sharply discontinuous at the boundaries between chambers.

Figure 3 presents corrections in one ring (ME-3/1) compared with measurements of the same parameter using other techniques. The  $\phi_y$  angles of chambers in all rings were measured using the tracker-propagation technique, while other methods were limited to different subsets of rings (ME-3/1 is the only ring in which all could be compared). From the raw residuals represented as a color scale in the plot, we can see discontinuities along

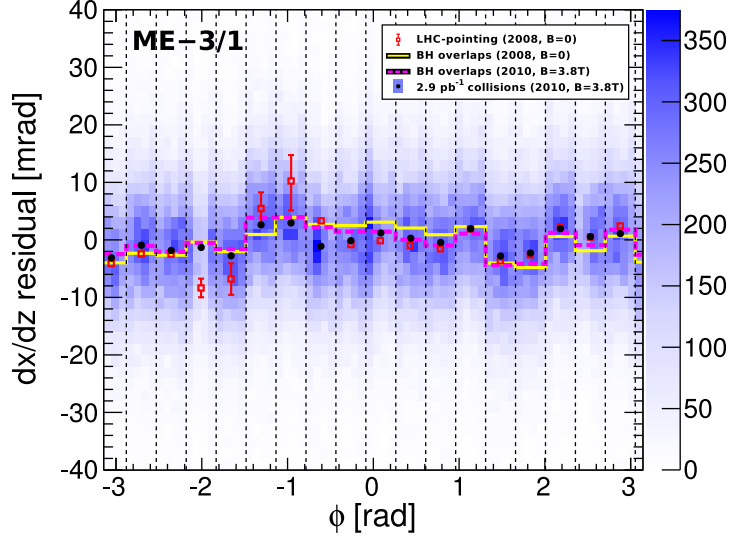


Figure 3: Comparison of  $\phi_y$  measurements using several different methods: zero-field beam-halo trajectories from the LHC beamline (red open squares), zero- and full-field measurements using tracks crossing the edges of CSCs (histograms), and entrance angle residuals from the tracker (black points and color-scale background). The color-scale represents the distribution of all residuals versus  $\phi$ , while the black points are average residuals per chamber.

the borders between chambers, demonstrating that the systematic differences are related to the chambers, rather than errors in track propagation. (It would be highly unlikely for propagations errors unrelated to the chambers to deviate exactly at the boundaries of the chambers.) The “LHC pointing” method assumes that beam-halo muons observed in zero magnetic field point back to a straight, infinitely long beamline. The “BH overlaps” (beam-halo overlaps) methods use beam-halo tracks passing through pairs of neighboring CSCs, much like the method described in the next section, but applied to  $\phi_y$  rather than  $x$  and  $\phi_z$ . Taken together, these measurements represent two years of  $\phi_y$  monitoring, yet they agree well at the level of 1–2 mrad.

## 4 Internal-ring alignment using beam-halo tracks

CSC chambers overlap slightly along their edges, and muons passing through these narrow regions provide information about the relative displacement of the neighboring chambers. Because of the short distances between the chambers and the lack of heavy material between them, straight-line propagations of the muon trajectory are precise at the level of 1.4 mm RMS (compared to tens of mm for tracks propagated from the tracker, depending on momentum). A systematic offset in the difference between track-segments propagated from each chamber to a plane equidistant between them (the “overlap residual”) is interpreted as a relative displacement between the two chambers (Fig. 4).

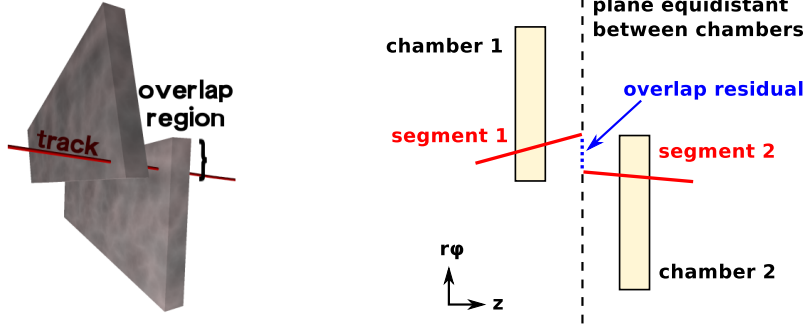


Figure 4: Relative alignment information from a muon passing through the overlap between two neighboring chambers.

To produce a complete geometry from the pairwise chamber information, the following objective function is minimized:

$$\chi^2 = \sum_{m_{ij}}^{\text{constraints}} \frac{(m_{ij} - A_i + A_j)^2}{\sigma_{ij}^2} + \lambda \left( \frac{1}{N_{\text{chambers}}} \sum_i^{\text{chambers}} A_i \right)^2 \quad (1)$$

where  $A_i$  are the chamber coordinates to optimize,  $m_{ij} \pm \sigma_{ij}$  are the pairwise chamber measurements, and  $\lambda$  is a Lagrange multiplier to compensate for the fact that the system has no external reference to define a coordinate system. Two chamber coordinates can be measured with high precision using this technique,  $r\phi$  (from an average offset in overlaps residuals) and  $\phi_z$  (from a trend in overlaps residuals as a function of local  $y$ ). Other coordinates are better measured with other methods. Only one coordinate is aligned at a time, alternating between  $r\phi$  and  $\phi_z$ .

Relative alignment information can only be propagated through a complete graph of alignment constraints, and since there are no overlaps between chambers in different rings, misalignments between rings are not corrected with this method. In addition, some rings are not fully connected due to one or two dead chambers or dead CFEs, affecting the region of overlap. In these rings, photogrammetry information is used to fill the gaps, with photogrammetry measurements introduced as constraints in Eqn. 1. Rings ME $\pm$ 1/1 have two missing chambers each, but no photogrammetry measurements to use as constraints. In this case, we measured the positions of the chambers neighboring the gaps with tracks from the tracker and applied them as constraints in the same way.

Figure 5 presents the results of this alignment by comparing post-alignment chamber positions to pre-alignment values from photogrammetry. Although photogrammetry information was used in the alignment, much larger weights were given to the beam-halo data. The level of agreement between the track-based technique and photogrammetry (0.3–0.6 mm) is smaller than the typical chamber corrections (2–3 mm).

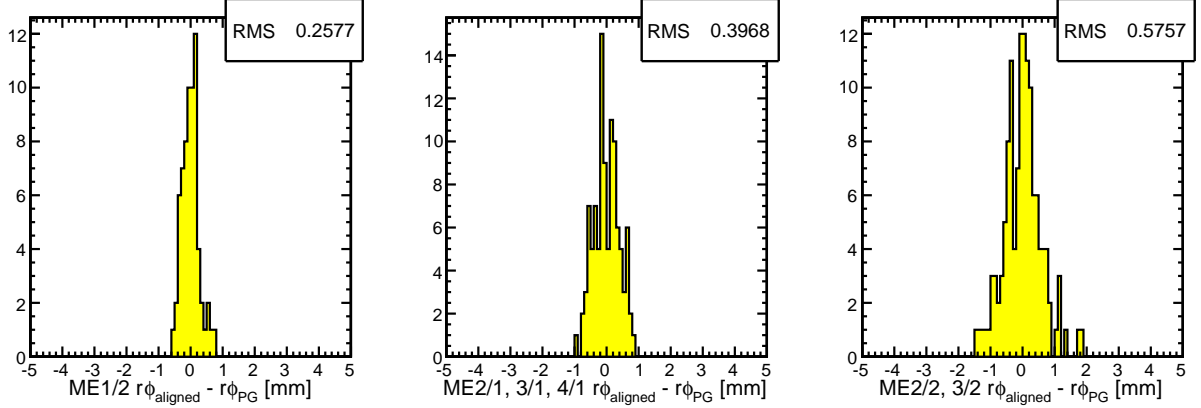


Figure 5: Chamber positions after internal-ring alignment compared with photogrammetry, split by ring. (ME1/1 chambers were not measured by the photogrammetry.)

## 5 Whole-ring placement using collisions muons

To complete the endcap alignment, the internally aligned rings must be aligned relative to one another and the tracker. Tracks from the tracker were propagated to the muon chambers and whole-ring corrections were derived from the pattern of  $r\phi$  residuals as a function of global  $\phi$ . A constant offset in the residuals is interpreted as a rotation of the ring in  $\phi_z$ , while terms proportional to  $\cos \phi$  and  $\sin \phi$  are interpreted as displacements in global  $x$  and  $y$ , respectively.

Figure 6 provides an example of an alignment fit for one ring (ME-2/1). The residuals distribution shows no apparent chamber-level misalignments in the form of discontinuities at the chamber boundaries. Residuals were fitted to truncated Gaussians to determine their peak positions in a way that is insensitive to non-Gaussian tails. Residuals from muons and antimuons were fitted separately and then averaged to reduced sensitivity to any errors in the magnetic field map, which would affect propagated tracks of opposite charges in opposite directions with equal magnitude. Finally, these points were fitted to

$$f(\phi) = c_0 + c_1 \cos \phi + c_2 \sin \phi \quad (2)$$

and  $c_0$ ,  $c_1$ ,  $c_2$  were used to align the rings. A second alignment pass was performed to verify the correction, and was found to be consistent.

To cross-check the alignment using a qualitatively different method, beam-halo tracks crossing an entire endcap (three or four stations, depending on distance from the beamline) were used to calculate residuals in one station relative to segments in another. Figure 7 shows an example, in which ME+3/1 segments were propagated linearly (no corrections for material or magnetic field) to ME+4/1. Residuals were fitted with truncated Gaussians in  $\phi$  slices, separately for muons and antimuons to correct for the magnetic field.

ME4/1 is the farthest station from the CMS tracker, and therefore if the alignment using tracks from the tracker is compromised by errors in track propagation, ME4/1 would experience the largest errors. On the other hand, the magnetic field is weakest in ME4/1, so the beam-halo method would have the smallest errors from linear track propagation and

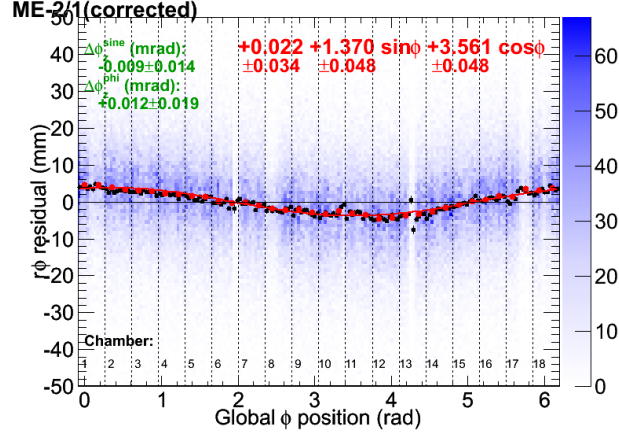


Figure 6: Residuals plot used to align a ring: the color scale is the residuals distribution versus  $\phi$ , black points are a profile derived from truncated-Gaussian peak fits in each  $\phi$  bin, and red points are the average of peak-fits to muons and antimuons separately. The fitted curve is interpreted as three alignment degrees of freedom. Vertical dashed lines indicate the boundaries between chambers.

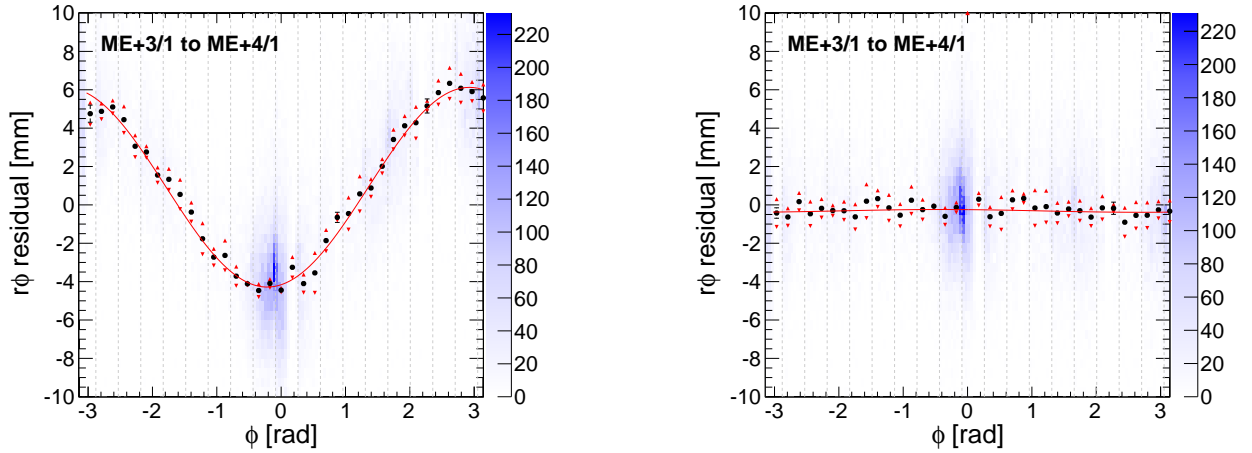


Figure 7: Residuals from beam-halo tracks used to cross-check the alignment performed with collisions. The symbols in these plots have the same meaning as Fig. 6, though residuals were calculated differently (see text). Left: before alignment. Right: after alignment using collisions (not beam-halo).

therefore be the most reliable in this station. As can be seen in Fig. 7, the beam-halo cross-check agrees with the tracker-track alignment at the level of 0.5 mm in ME+4/1 (and 0.3 mm in ME−4/1, not shown), establishing an upper bound on ring position errors of 0.5 mm throughout the endcap.

## 6 Conclusions

The endcap muon system was aligned using several complementary techniques. These alignments provide a precise geometry for CMS tracking and a baseline for comparison with future alignment techniques.